Zhang *et al. Biochar* (2026) 8:113
https://doi.org/10.1007/s42773-026-00634-8

Biochar

ORIGINAL RESEARCH Open Access

In situ observation of $Co_3O_{4-\alpha}$–OH formation on optimized biochar for peroxymonosulfate activation and ultrafast antibiotics degradation

Jian Zhang[1,2], Jiafang Xie[1,2*], Shuhui Zhu[1,2], Jiacheng E. Yang[1,2], Bo Weng[1,2] and Yuming Zheng[1,2]

Abstract

Biochar optimized with oxygen-containing functional groups is believed to be beneficial for peroxymonosulfate (PMS) activation, and biochar-loaded Co_3O_4-based catalysts are expected to be one of the most promising PMS activators for the efficient removal of organic pollutants. Nevertheless, the real active sites on Co_3O_4 catalysts are still in debate due to insufficient experimental evidence. Herein, Co_3O_4 growing on the oxygen-containing functional groups optimized rice husk biochar (RHBA) was synthesized (RHBA@Co_3O_4), and RHBA800@25Co_3O_4 + PMS system achieved complete degradation (100%) of refractory levofloxacin (LFX) within 4 min. The superior catalytic performance was suggested to be attributed not only to the uniform dispersion of Co_3O_4, but also to the transformation of lattice oxygen in Co_3O_4, which was found to play an important role in the catalytic process by inducing the formation of $Co_3O_{4-\alpha}$–OH. Meanwhile, density functional theory (DFT) calculations indicated that the adsorption energy (E_{ads}) of PMS on $Co_3O_{4-\alpha}$–OH was far lower than that on Co_3O_4. Moreover, both radical and non-radical pathways were indicated to be involved during the degradation process. Additionally, the practical application of RHBA@Co_3O_4 was investigated using various antibiotics, actual water environments, and fixed-bed reactors. The results showed that it possessed good practical degradation performance and significantly reduced the toxicity of intermediate products. This work provides a fresh insight into the catalytic mechanism of RHBA800@25Co_3O_4 for PMS activation and wastewater treatment, offering a new perspective on the catalytic mechanism of Co_3O_4-based materials.

Highlights

- RHBA800@25Co_3O_4 exhibited ultrafast antibiotics degradation via peroxymonosulfate activation.
- Inspired formation of $Co_3O_{4-\alpha}$–OH by lattice oxygen induction was explored.
- Ecological safety of levofloxacin degradation products was verified through antibacterial experiments.

Keywords Optimized biochar, Co_3O_4 catalyst, Peroxymonosulfate, Antibiotics degradation, Environmental sustainability

*Correspondence:
Jiafang Xie
jfxie@iue.ac.cn
Full list of author information is available at the end of the article

Springer

Graphical Abstract

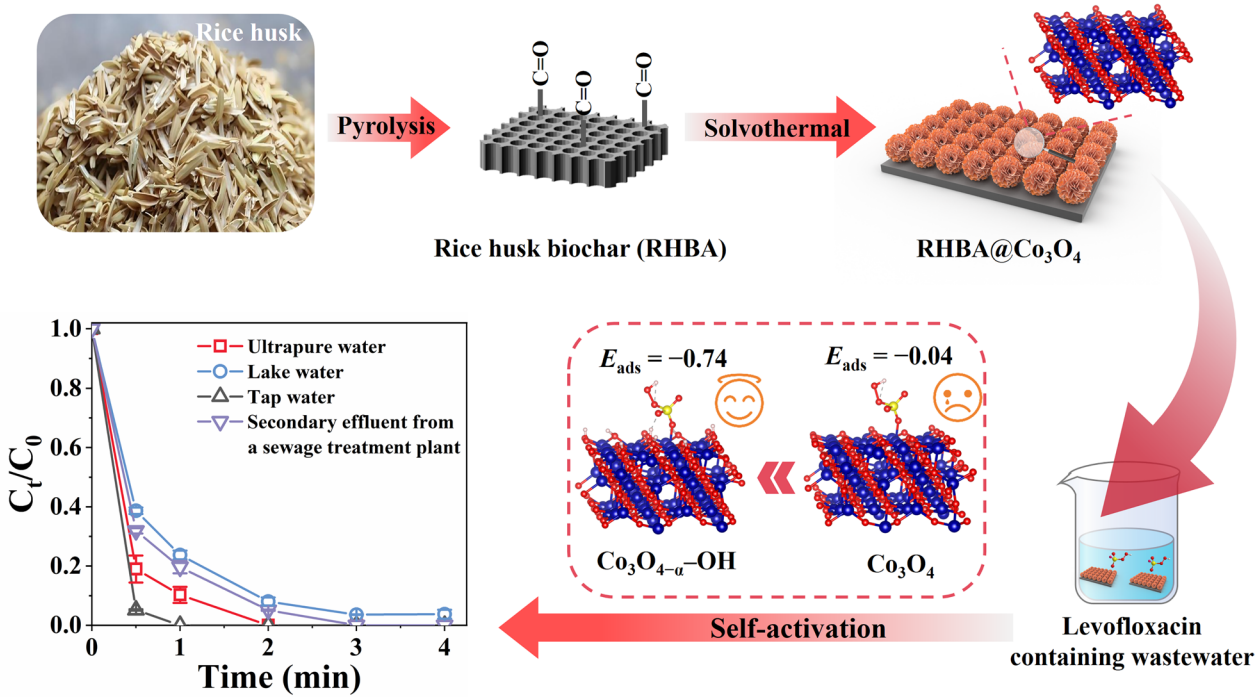

1 Introduction

Water pollution by the emerging contaminants, such as pharmaceuticals and personal care products (especially antibiotics), endocrine-disrupting compounds, and pesticides is of increasing concern due to their potential toxicity and persistence (Wang et al. 2024a; Meena et al. 2025). Antibiotics are typically not fully metabolized within organisms, with approximately 70% being excreted directly into the environment (Georgin et al. 2024). More critically, fluoroquinolone antibiotics have been detected in municipal wastewater at concentrations ranging from ng L^{-1} to μg L^{-1}, and even reaching mg L^{-1} in pharmaceutical wastewater (Oberlé et al. 2012). Levofloxacin (LFX), a common fluoroquinolone antibiotic, accounted for 44.3% of the total antibiotics detected in drinking water in China (Wang et al. 2024a, b). However, conventional wastewater treatment plants are ineffective at removing LFX, leading to its entry into aquatic ecosystems and posing serious threats to both natural ecology and human health (Weng et al. 2025). Therefore, it is imperative to develop effective methods for removing LFX from wastewater.

Advanced oxidation processes (AOPs), involving peroxymonosulfate (PMS)-activated Fenton-like catalysis with significant reactivity against most refractory organic pollutants, have been considered a promising strategy for the restoration of organically contaminated systems (Li et al. 2024b; Zhao and Zhang 2025). It can be easily activated by both homogeneous and heterogeneous catalysts, and the generated $SO_4^{\cdot-}$ possesses a high redox potential (2.5–3.1 V) and relatively longer lifetime (30–40 μs) compared to the main ·OH (1.8–2.7 V, 20 ns) produced by the traditional H_2O_2 AOPs (Patil and Grewal 2025). At present, AOPs catalysts mainly include carbonaceous materials, noble metals, and transition metal oxides (Zhang et al. 2024; Yu et al. 2024). Among them, transition metals oxides are widely applied to activate persulfate to degrade organic pollutants ascribed to the high efficiency of charge transfer and earth-abundant existence, and cobalt oxide (Co_3O_4) coupled with PMS has been demonstrated to be a highly effective process for the generation of $SO_4^{\cdot-}$ because of its excellent catalytic performance and stability (Wang et al. 2025). However, Co_3O_4 also has some drawbacks, such as the agglomeration of Co_3O_4 nanoparticles, which can lead to a decrease in catalytic activity, and the inevitable leaching of cobalt ions (Gao et al. 2025). These would not only inhibit the exposure of active sites for catalysis, but also lead to secondary pollution in the

treated water. To overcome the shortcomings, various supporting materials for loading Co_3O_4 have been attempted to improve the stability and the catalytic performance, such as metal oxides, molecular sieves, and carbon materials.

Biochar is a carbonaceous material produced from the pyrolysis of carbon-rich biomass waste with high porosity, stability, and conductivity (Ji et al. 2021). Rice husk is a major agricultural by-product generated globally in enormous quantities, and its utilization for biochar production aligns perfectly with the principles of waste valorization and circular economy. The porous structure of biochar makes it a promising support for metal and metal oxide nanoparticles and enhances their specific surface area, thereby increasing their catalytic activity for PMS activation. Meanwhile, the surface functional groups of biochar may interact with nanoparticles and thus improve the dispersion and stabilization of them (Huang et al. 2024). In addition, the oxygen-containing functional groups distributed on biochar surface, such as C–O, C=O, and O–H groups, can also be applied as activators for PMS, especially the C=O group could degrade organic pollutants via generating singlet oxygen ($^1O_2$) (Tian et al. 2025). Therefore, the regulation of oxygen-containing functional groups on biochar surface via different calcination temperature is crucial for the loading of Co_3O_4 and the improvement of catalytic performance. However, the contribution to PMS activation by biochar-loaded Co_3O_4 has been attributed mainly to its high dispersibility and redox potential, and the catalytic mechanism remains unclear. This study attempts to prepare highly efficient PMS catalysts through the optimization of surface oxygen-containing functional groups and to explore the unclear catalytic mechanisms.

In this work, appropriate Co_3O_4 with spherical shape was uniformly dispersed on the oxygen-containing functional group-regulated biochar derived from rice husk (RHBA@Co_3O_4), and the fabricated catalyst was applied to activate PMS for radicals' generation. LFX, a typical fluoroquinolone antibiotic of emerging organic contaminant, was selected as a model pollutant due to its abuse and incomplete metabolism in organisms. Meanwhile, various advanced techniques such as HAADF-STEM, in situ Raman, in situ FT-IR, and XPS were employed to explore the catalytic mechanism. The main objectives of this study are as follows: (I) Construction of an oxygen-containing functional group-optimized biochar for ultrafast antibiotic removal; (II) Revelation of the insightful catalytic mechanism on Co_3O_4 for PMS activation; (III) Evaluation of the catalytic performance in practical applications with different antibiotics, actual water, and a self-developed fixed-bed reactor.

2 Materials and methods

2.1 Chemicals

Rice husks were provided by a rice processing factory in Wenzhou City, China. Levofloxacin (LFX), peroxymonosulfate ($KHSO_5{\cdot}0.5KHSO_4{\cdot}0.5K_2SO_4$, PMS), p-benzoquinone (p-BQ), and furfuryl alcohol (FFA) were provided by Shanghai Aladdin Biochemical Technology Co., Ltd. Cobaltous nitrate hexahydrate ($Co(NO_3)_2{\cdot}6H_2O$), formic acid, methyl phenyl sulfoxide (PMSO), and methyl phenyl sulfone ($PMSO_2$) were provided by Shanghai Macklin Biochemical Co., Ltd. Ammonium hydroxide ($NH_3{\cdot}H_2O$) was supplied by Xilong Scientific Co., Ltd. Ethylene glycol, tert-butanol (TBA), and ethanol (EtOH) were purchased from Sinopharm Chemical Reagent Co., Ltd. Acetonitrile and methanol were purchased from Oceanpak Alexative Chemical Co., Ltd. 5,5-Dimethyl-1-Pyrroline-N-oxide (DMPO) and 4-Amino-2,2,6,6-tetramethylpiperidine (TEMP) were purchased from Sigma-Aldrich (Shanghai) Trading Co., Ltd. All of the chemicals used in this experiment were analytically pure and required no further purification.

2.2 Synthesis of catalysts

2.2.1 Preparation of RHBAx

In this work, rice husks were first cleaned thoroughly with deionized water several times to remove impurities and dried at 80 °C for 24 h. Afterwards, the dried rice husks were placed in a tube furnace and carbonized at 700 °C for 2 h with a heating rate of 4 °C min^{-1} under N_2 atmosphere. The obtained carbonized rice husks were ground and sieved to obtain an even size (<75 μm) and named as RHB. Then, 3.0 g of RHB and 6.0 g of KOH were added into 107 mL ultrapure (UP) water for 30 min sonication; the mixture was evaporated at 120 °C with vigorous stirring. Subsequently, the KOH-impregnated RHB was placed in a tube furnace and activated at a higher temperature (700, 800, and 900 °C) for 2 h with a heating rate of 4 °C min^{-1} under N_2 atmosphere. Finally, the activated RHB was neutralized using HNO_3 solution (1 M) and washed to neutrality by filtration with UP water. The resultant product was dried in an oven at 80 °C and abbreviated as RHBAx (x = 700, 800, and 900, respectively, representing the activation temperature).

2.2.2 Preparation of RHBAx@yCo3O4

Co_3O_4-loaded RHBA was synthesized according to the classical solvothermal method (Song et al. 2023). Briefly, a certain amount (0.16, 0.48, and 1.12 g) of RHBAx and 0.582 g of $Co(NO_3)_2{\cdot}6H_2O$ were added into 35 mL of

ethylene glycol under vigorous stirring. After 20 min of agitation, 2 mL of $NH_3{\cdot}H_2O$ (26.00 wt%) was added to continue stirring for 10 min. Then, the mixture was transferred into a Teflon-lined stainless-steel autoclave and heated at 160 °C for 12 h. After the completion of the reaction, the product was washed six times by centrifugation with anhydrous ethanol and UP water alternately. After drying in an oven at 60 °C, the materials were annealed in a tube furnace at 350 °C for 2 h with a heating rate of 4 °C min^{-1} under air atmosphere. The final products were denoted as RHBAx@yCo_3O_4 (y represents the mass percentage of theoretical Co_3O_4 loading). Meanwhile, Co_3O_4 was prepared using the same method without the addition of RHBAx. A schematic diagram of the catalyst preparing procedure is shown in Fig. 1a.

2.3 Experimental procedure

LFX stock solution was simply prepared using UP water with an initial concentration of 10 mg L^{-1} and initial pH of 6.5 ± 0.1. The experiments were conducted in a 250-mL beaker containing 100 mL of LFX solution with constant magnetic agitation at 25 °C. Typically, 5 mg of catalyst was poured to the target LFX solution and stirred for 10 min in dark for complete adsorption. Subsequently, 0.15 mM PMS was added to initiate the degradation experiment. At predetermined time intervals (0, 0.5, 1, 2, 3, and 4 min), the reaction solution (1 mL) was extracted and rapidly terminated by anhydrous ethanol (1 mL) to prevent further reaction, followed by immediate filtration using a 0.45-μm polyethersulfone (PES) membrane before analysis. All experiments were repeated twice and the average data were reported.

2.4 Characterizations and analytical methods

Details for the characterizations (Text S1) and analytical methods (Text S2–S6) are specifically described in the Supporting Information.

3 Results and discussion

3.1 Characterizations of RHBAx@yCo_3O_4

The morphology and microstructure of RHB, RHBAx, and RHBAx@yCo_3O_4 were observed by SEM and TEM. As presented in Fig. S1, RHB and RHBAx exhibited mostly blocky shapes, with a large number of pore channels distributed on the cross-section. In addition, finer pores appeared with the increase of activation temperature. After the decoration of Co_3O_4 with nanoflake structure (Fig. S2), a large amount of flower-like nanoflakes were observed in RHBA800@12.5Co_3O_4 (Fig. S3a). These flower-like Co_3O_4 nano-spheres uniformly grew on the RHBA800 surface, with a diameter of about 200 nm and a thickness of less than 5 nm. However, the surface morphology changed significantly with increasing Co_3O_4 loading. As for RHBA800@25Co_3O_4, Co_3O_4 still exhibited a flower-like morphology with thin flakes (Fig. S3b), while Co_3O_4 exhibited a granular morphology in RHBA800@50Co_3O_4 (Fig. S3c). This may be mainly due to the change in morphology caused by the increased loading amount.

To further explore the structure and morphology of the materials, TEM was conducted. Figures 1b and 1c exhibit neat images of RHBA800@25Co_3O_4; it can be found that Co_3O_4 is distributed in the outer layer and its edges are clean. Besides, the HRTEM image shows the lattice fringe of 0.194 nm in Fig. 1d, and the corresponding diffraction ring of plane (400) was also observed in SAED images (Fig. S4) (Jiang et al. 2014). Besides, the HAADF-STEM and elemental mapping of RHBA800@25Co_3O_4 are presented in Fig. 1e with a uniform distribution of C, O, and Co in the catalyst, indicating an even dispersion of Co_3O_4.

Nitrogen adsorption–desorption isotherms and pore size distributions of RHB, RHBAx, Co_3O_4, and RHBAx@yCo_3O_4 were determined and the results are presented in Fig. 1f and Fig. S5. It can be observed that the isotherm of RHB is type I based on the classification of BDDT (Braunauer, Deming, and Teller) (Zou et al. 2021), characteristic of a microporous material. The isotherms of Co_3O_4, RHBAx, and RHBAx@yCo_3O_4 are type IV with mesoporous characteristics, and exhibited hysteresis types of H3, H2, and H4, respectively, according to IUPAC classification (Schlumberger and Thommes 2021). These results indicated that RHBAx@yCo_3O_4 materials do not have distinct mesoporous structures. As listed in Table S1, the specific surface areas (S_{BET}) of RHBAx increased with the increase of activation temperature, while the S_{BET} of RHBA800@yCo_3O_4 decreased with the loading amount of Co_3O_4. Meanwhile, the total pore volume (V_{Total}) showed the similar tendency with S_{BET}. Furthermore, Fig. S6 shows the pore size distribution of these materials calculated using the non-localized density functional theory (NLDFT) method. RHB and RHBAx exhibited a main pore size distribution below 2 nm, suggesting that these materials are predominantly microporous. However, after being loaded with mesoporous Co_3O_4, the average pore diameter (D_{ap}) gradually increased as the loading amount increased. These results suggested that Co_3O_4 has been successfully decorated on RHBA800 surface, and the morphology has been significantly changed with the reduction of S_{BET} and V_{Total}.

FT-IR spectra of RHB, RHBAx, Co_3O_4, and RHBA800@yCo_3O_4 are exhibited in Fig. 1g and Fig. S7. It was observed that all the samples exhibited a broad absorption peak located at 3447 cm^{-1}, which was ascribed to the O–H stretching vibrations obtained

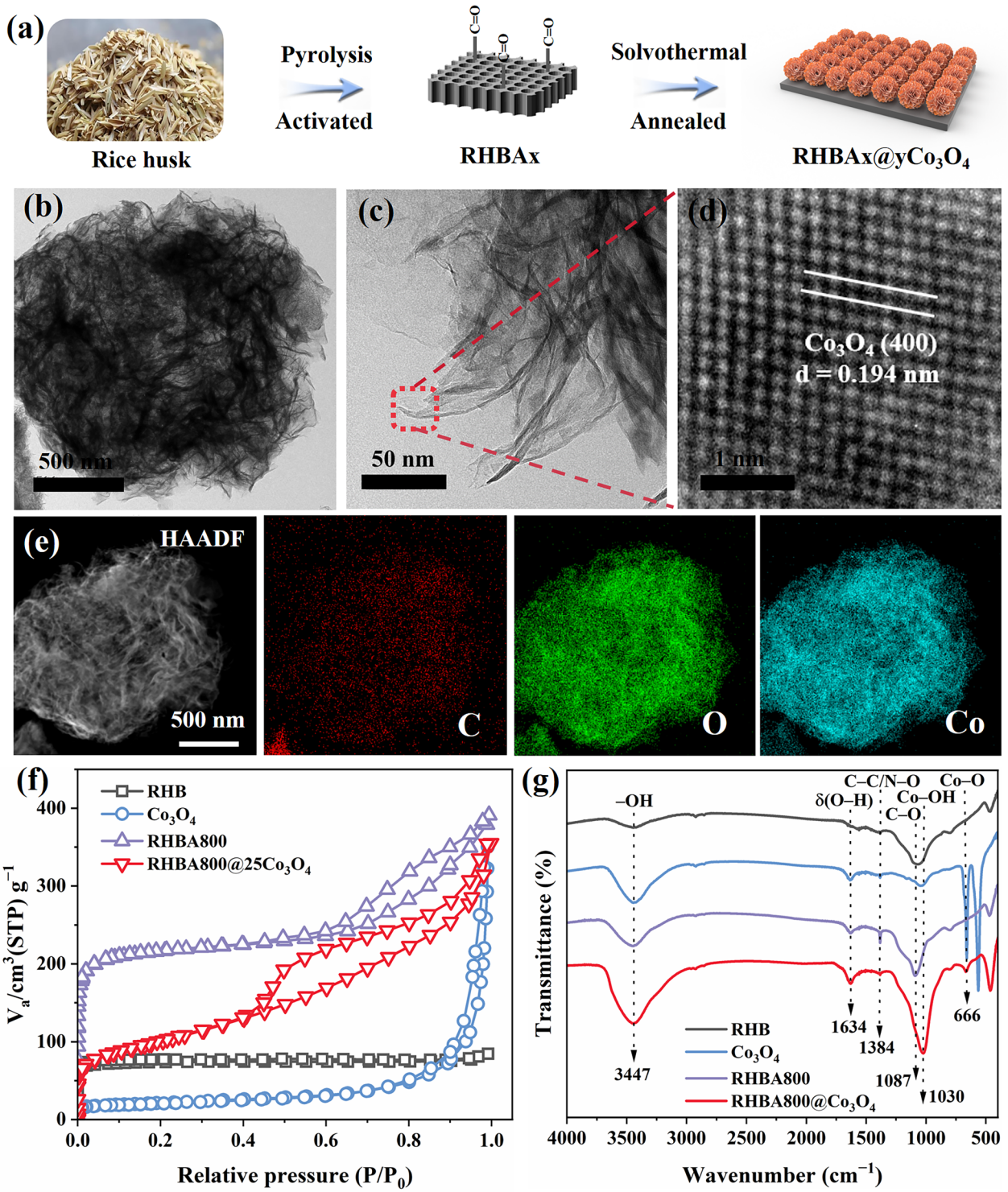

Fig. 1 **a** A schematic diagram of the preparing procedure for RHBAx@yCo_3O_4; **b–d** TEM images of RHBA800@25Co_3O_4; **e** HAADF-TEM images and element mappings of C, O, and Co of RHBA800@25Co_3O_4; **f** Nitrogen adsorption–desorption isotherms of RHB, Co_3O_4, RHBA800, and RHBA800@25Co_3O_4; **g** FT-IR spectra of RHB, Co_3O_4, RHBA800, and RHBA800@25Co_3O_4

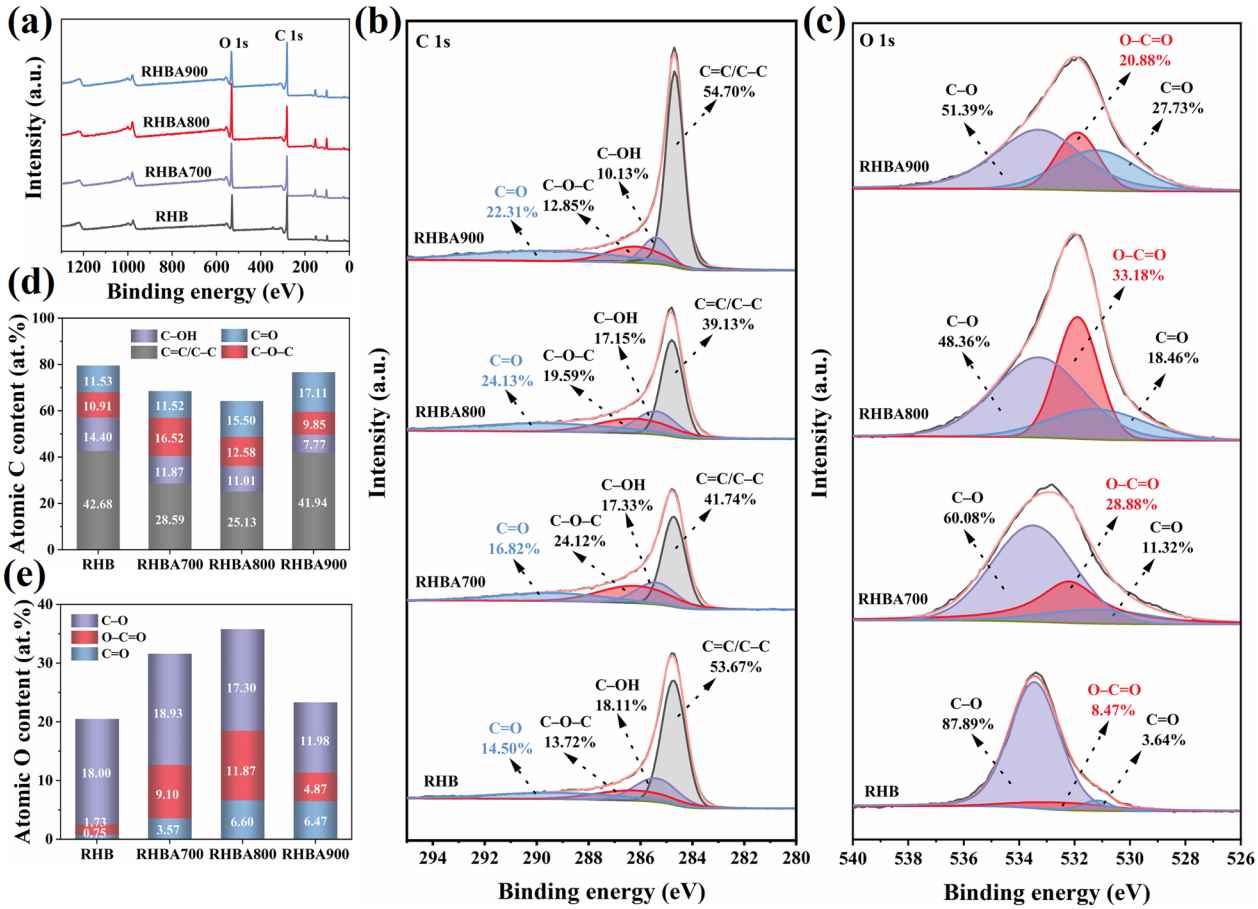

Fig. 2 XPS spectra of **a** survey, **b** C 1s, **c** O 1s, **d** atomic C content, and **e** atomic O content for RHB and RHBAx

from the hydroxyl groups and interlayer water molecules (Bao et al. 2025). In the spectra of RHB and RHBAx, the 2923 and 2852 cm^{-1} peaks corresponded to stretching vibrations of $-CH_2$ in alkyl groups. As exhibited, there was a characteristic peaks located at 1634 cm^{-1}, which belonged to the shearing vibration of water molecules (Hu et al. 2021; Chen et al. 2024a). In addition, there was a sharp absorption peak centered at 1087 cm^{-1}, which was ascribed to the stretching vibration of C–O. Additionally, the absorption peak at 803 cm^{-1} was due to the out-of-plane vibration of aromatic C–H in cellulose and carbohydrates (Bhagia et al. 2022). After the modification of Co_3O_4, there were two new absorption peak observed at 666 and 563 cm^{-1}, corresponding to the stretching vibrations of Co–O bonds (Song et al. 2023). Remarkably, the peak intensity of Co–O stretching vibration increased significantly with the increase of Co_3O_4 loading amount, suggesting the successful combination of Co_3O_4 and RHBA. Besides, XRD characterizations also demonstrated the successful decoration of Co_3O_4, owing to the appearance of new diffraction peaks belonging to Co_3O_4 (Text S10 and Fig. S8).

The surface chemical environment and oxygen-containing functional groups on RHBAx prepared from different calcination temperatures were investigated via XPS spectra. As shown in Fig. 2a, the characteristic peaks of C 1s and O 1s were observed. Figure 2b displays the deconvoluted C ls spectra at the binding energies of 284.8, 285.4, 286.2, and 289.2 eV, which corresponded to C=C/C–C, C–OH, C–O–C, and C=O, respectively (Wang et al. 2022). Similarly, the O 1s in Fig. 2c could be identified as C=O, O–C=O, and C–O at the binding energies of 531.2, 531.9, and 533.3 eV, respectively (Li et al. 2022). In addition, the total C and O contents were analyzed, and the specific proportions of the groups were compared (Fig. 2d). As exhibited, the C–O–C content increased after the activation and then decreased with the carbonization temperature. Meanwhile, the C–OH content decreased from 11.87 at.% (RHBA700) to 7.77 at.% (RHBA900). In contrast, the content of C=O gradually increased with the carbonization

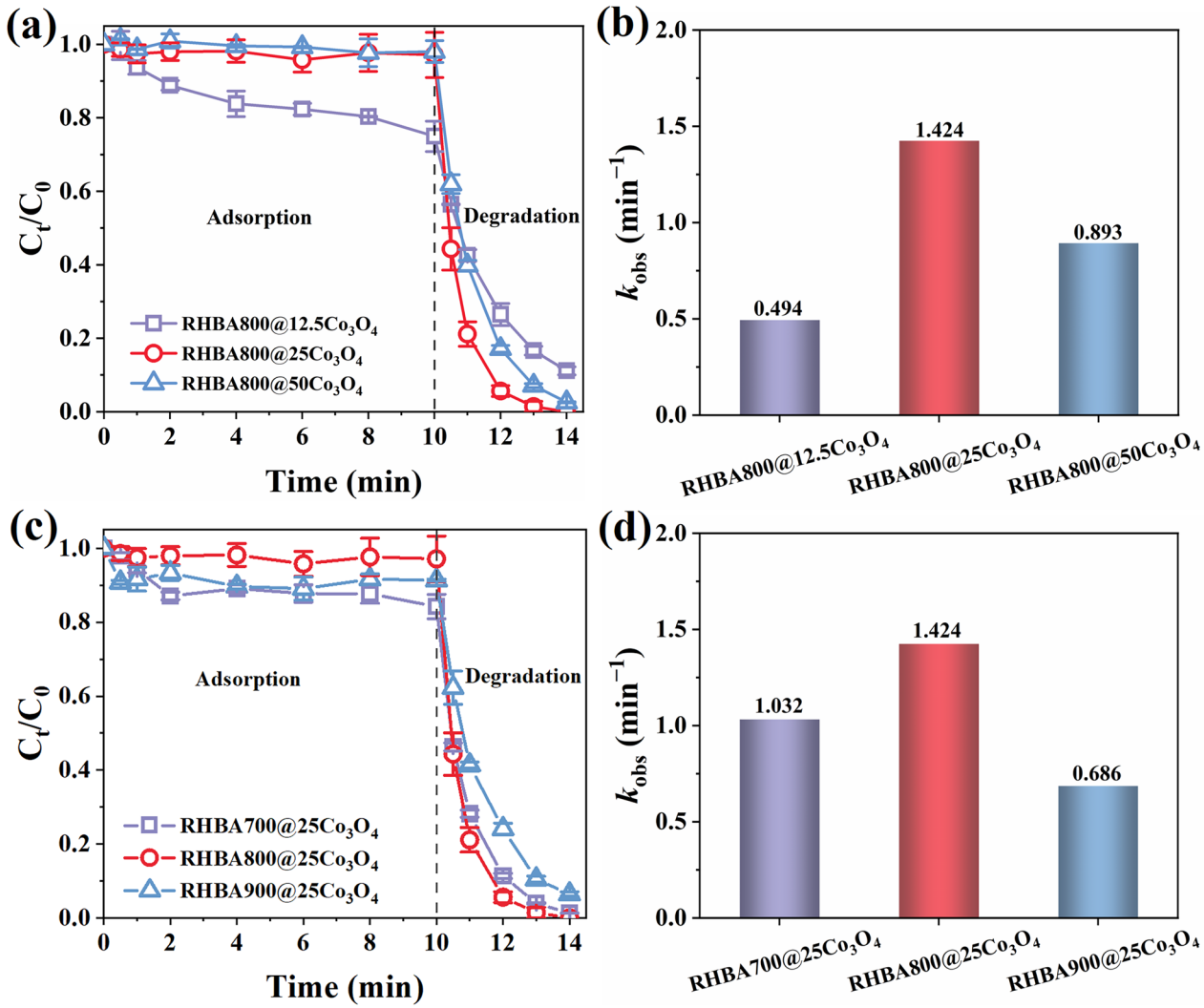

Fig. 3 **a**, **c** Degradation efficiency and **b**, **d** pseudo-first-order kinetics fitting of LFX in the different systems (Experimental conditions: $[Catalysts]_0 = 0.05$ g $L.^{-1}$, $[PMS]_0 = 0.15$ mM, $pH_0 = 6.5$, $T = 25$ °C)

temperature, which can be ascribed to the conversion of C–O during the heating treatment. Moreover, the O–C=O content decreased with the increase of carbonization temperature, and the C–O content also gradually decreased from 18.93 at.% for RHBA700 to 11.98 at.% for RHBA900 (Fig. 2e). Noticeably, the C=O content achieved a higher proportion in RHBA800 (6.60 at.%) and RHBA900 (6.47 at.%) than in RHB (0.75 at.%) and RHBA700 (3.57 at.%). This might be due to a large amount of C=O produced during the activation process and the high temperature facilitating the conversion of C–O to C=O, which would be conducive to $^1O_2$ generation during PMS activation.

3.2 Comparison of degradation performance for RHBAx@yCo_3O_4

To validate the excellent catalytic performance of RHBA800@$25Co_3O_4$, experiments were conducted to degrade LFX by activating PMS in different systems. As presented in Fig. S9, the degradation performance of Co_3O_4 and RHBA was relatively low, and the adsorbed LFX was suggested to be released from the materials with the addition of PMS. However, the degradation efficiency of RHBAx@yCo_3O_4 was significantly improved with the addition of PMS after adsorption (Fig. 3a, c). As exhibited, RHBA800@$25Co_3O_4$ achieved a higher degradation efficiency (100%) within 4 min than RHBA800@$12.5Co_3O_4$ (88.86%) and RHBA800@$50Co_3O_4$ (97.41%). In addition, the catalytic performance of RHBAx@$25Co_3O_4$ was compared, and

RHBA800@25Co_3O_4 exhibited the best degradation performance, outperforming RHBA700@25Co_3O_4 (98.69%) and RHBA900@25Co_3O_4 (93.56%). Meanwhile, the residual PMS concentration was determined (Fig. S10), showing that RHBA800@25Co_3O_4 exhibited the highest PMS consumption. The results suggested that the catalytic capacities of pure Co_3O_4 and RHBA were relatively limited. As for the pure Co_3O_4, the serious aggregation caused by high surface energy greatly hindered the catalytic capacity. After the uniform dispersion of Co_3O_4 on the RHBA surface, the highly dispersed tiny Co_3O_4 nanoflakes can expose more active sites. Meanwhile, the porous structure and surface chemical environment of RHBA can also influence the catalytic performance.

Furthermore, to precisely assess the degradation kinetics, a pseudo-first-order kinetics model was used to describe the degradation processes (Text S5). As exhibited in Fig. 3b, d, the obtained kinetics rate constants (k_{obs}) for different systems were in the order of RHBA800@25Co_3O_4 (1.424 min^{-1}) > RHBA700@25Co_3O_4 (1.032 min^{-1}) > RHBA800@50Co_3O_4 (0.893 min^{-1}) > RHBA900@25Co_3O_4 (0.686 min^{-1}) > RHBA800@12.5Co_3O_4 (0.494 min^{-1}), which was in line with the LFX degradation performance of these catalysts. Meanwhile, a comparative study of antibiotics degradation across different catalysts revealed that RHBA800@25Co_3O_4 exhibited higher k_{obs} and degradation efficiency with low catalyst and PMS dosage (Table S2), further confirming its outstanding catalytic activity and ultrafast degradation efficiency towards antibiotics. Moreover, the effects of catalyst dosage, PMS dosage, initial solution pH, and even the influence of co-existing ions were thoroughly investigated in the Supporting Information (Text S11–S14 and Fig. S11–S14), confirming that RHBA800@25Co_3O_4 + PMS could be a prominent system for LFX degradation.

3.3 Identification of reactive oxygen species (ROS) and activation mechanisms

3.3.1 Identification of ROS

To investigate the ROS that generated in the RHBA800@25Co_3O_4 + PMS system, different quenchers were employed to capture the ROS during the LFX degradation process (Wang et al. 2021; Chen et al. 2024b). As exhibited in Fig. 4a, b , EtOH, TBA, and FFA exhibited significant inhibitory effects on the degradation of LFX, while p-BQ showed weak inhibitory effect on it. Correspondingly, the signals of DMPO-$SO_4^{\cdot-}$ and DMPO-·OH were detected with in situ electron

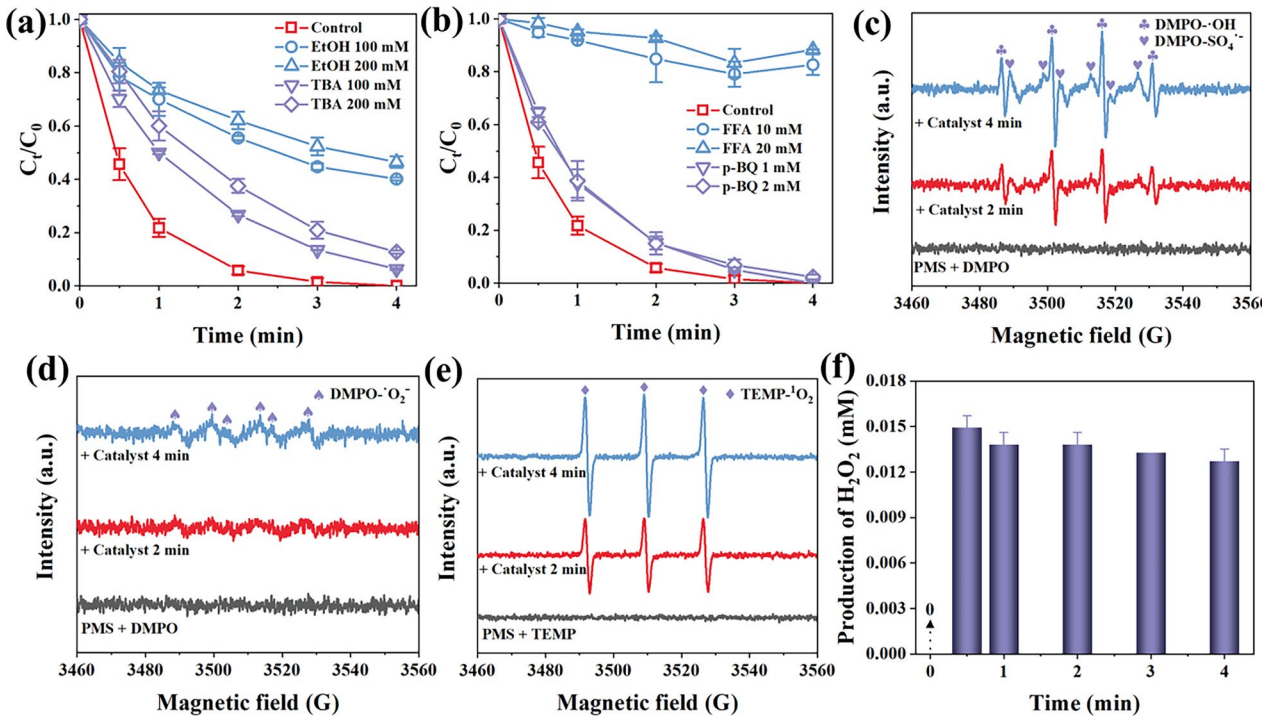

Fig. 4 Effects of **a** EtOH, TBA, **b** p-BQ, and FFA scavengers on LFX degradation in RHBA800@25Co_3O_4 + PMS system; In suit EPR spectra of **c** $SO_4^{\cdot-}$/·OH, **d** $\cdot O_2^-$, and **e** $^1O_2$ with the addition of DMPO and TEMP in RHBA800@25Co_3O_4 + PMS system; **f** Production of H_2O_2 in RHBA800@25Co_3O_4 + PMS system (Experimental conditions: $[Catalysts]_0$ = 0.05 g L^{-1}, $[PMS]_0$ = 0.15 mM, pH_0 = 6.5, $[LFX]_0$ = 10 mg L^{-1}, $[DMPO]_0 = [TEMP]_0$ = 50 mM)

paramagnetic resonance (EPR) in Fig. 4c, indicating that the degradation process of LFX was attributed to both $SO_4^{\cdot-}$ and ·OH. In addition, the intensity of the signals increased over time within 4 min, further illustrating an efficient and persistent activation in the RHBA800@25Co_3O_4 + PMS system. Meanwhile, the relatively weak signals of DMPO-$^{\cdot}O_2^-$ were detected (Fig. 4d), indicating the negligible presence of $^{\cdot}O_2^-$. Surprisingly, an apparent signal of triple peaks with an intensity ratio of 1: 1: 1 was found (Fig. 4e), implying the existence of $^1O_2$ during PMS activation (Chen et al. 2022). Moreover, the intensity of $^1O_2$ signal increased with the reaction proceeding, verifying that the process generated $^1O_2$ continuously through the strong interaction between PMS and RHBA800@25Co_3O_4. Combined with the quenching experiment of FFA, it was speculated that $^1O_2$ accounts for a large proportion during the reaction process. Meanwhile, H_2O_2 was detected in the PMS activation process (Fig. 4f), which could produce $HO_2^{\cdot-}$ to facilitate the generation of $^1O_2$ (Text S15). Besides, the high-valent metal-oxo species were detected using PMSO as the scavenger with a low transformation efficiency of $PMSO_2$ (Fig. S15), which indicated that high-valent metal-oxo species were negligible (Lu et al. 2025).

3.3.2 Possible activation mechanism in RHBA800@25Co3O4 + PMS system

In situ Raman was applied to reveal the interactions between RHBA800@25Co_3O_4 and PMS (Fig. 5a and Fig. S16). As observed, the peaks located at 881 and 1059 cm^{-1} were attributed to the O–O bond and SO_3^- in PMS, respectively, and the peak at 981 cm^{-1} was assigned to the symmetric stretching vibrational mode of the S=O bond in SO_4^{2-} (Zhang et al. 2025a). Remarkably, the RHBA800@25Co_3O_4 + PMS system exhibited a new peak at 834 cm^{-1} compared to the PMS alone system, which was suggested to be the formation of peroxo-species bonding to the metal sites on catalyst surface (referred as metal-PMS*) (Li et al. 2024a, b). Meanwhile, it was noteworthy that the peak of SO_3^- in PMS split into two small peaks at 1053 cm^{-1} (red shift) and 1071 cm^{-1} (blue shift), suggesting that electron transfer occurred between the asymmetric sites of PMS and the orientation may be different (Mo et al. 2023). The red shift typically originated from the enhancement of electron density, indicating the donation of electrons from catalysts to PMS. Finally, the peaks of O–O, SO_3^- and PMS* weakened with the addition of LFX, indicating the rapid PMS activation and consumption.

Meanwhile, the in situ FT-IR spectra of PMS presented obvious absorption peaks at 602 and 1103 cm^{-1} (Fig. S17), which were ascribed to the S–O and S=O=S tensile vibrations of HSO_5^-, respectively (Zhou et al. 2023). After RHBA800@25Co_3O_4 was mixed, there was a blue shift about 14 and 4 cm^{-1} for the corresponding peaks due to the increase in electron density of the S–O bond in HSO_5^-. Accordingly, the chronopotentiometry curves in Fig. 5b showed that the potential increase in the presence of PMS, followed by a gradual decrease upon the addition of LFX. Meanwhile, the amperometric i–t curves showed the nosedive phenomenon with the addition of PMS and LFX (Fig. S18). These results suggested that the electron exchange between RHBA800@25Co_3O_4 and PMS occurred intensively, and that LFX diffused onto the catalyst surface and reacted with the surface-activated PMS due to the fast electron transfer. Moreover, the in situ FT-IR spectra of the catalyst exhibited that the Co–OH absorption peak at 1035 cm^{-1} was gradually enhanced during the reaction (Fig. 5c and Fig. S19) (Gong et al. 2023), which was consistent with the Co–OH peak appearing in in situ Raman spectra. These results indicated that the chemical environment on the surface of the catalyst was significantly altered.

XPS was applied to further investigate the surface chemical environment of RHBA800@25Co_3O_4 before and after degradation (Fig. S20a), and the spectra of C 1s, O 1s, and Co 2p were explored. As observed, the area ratio of C=O decreased from 22.27% to 15.64% after the degradation (Fig. S20b), which was mainly due to the involvement of O–C=O on the RHBA surface during the LFX degradation process. In contrast, the area ratios of C–OH (285.3 eV) and C–O–C (286.1 eV) increased after the degradation, which was primarily ascribed to the transformation from C=O and C–C groups (Wang et al. 2022). Meanwhile, the O 1s spectrum changed a lot after the degradation. As exhibited in Fig. 5d, there was no obvious change for adsorption oxygen (O_{ads}) caused by the water molecule adsorption. Meanwhile, the area ratio of lattice oxygen O^{2-} (O_{latt}) derived from Co–O at 529.4 eV decreased from 60.08% to 21.86% (Chen et al. 2019), and the surface oxygen (O_{surf}) attributed to the hydroxyl group (–OH) and oxygen vacancy (O_{vac}) at 530.7 eV significantly increased from 37.90% to 76.13% (Zhao et al. 2021). Nevertheless, the O_{vac} did not change much after degradation via the EPR test (Fig. S21), demonstrating that the increase of O_{surf} was mainly due to the formation of –OH on the catalyst surface. Therefore, it was suggested that both of O_{latt} and O_{ads} participated in the redox and electron transfer in the RHBA800@25Co_3O_4 + PMS system, and that O_{latt} played a major role in the rapid induction of "Co_3O_4–OH" intermediate (represented as $Co_3O_{4-\alpha}$–OH). Finally, there was almost no change in Co^{3+} and Co^{2+} area ratios from the comparison of Co 2p spectra in Fig. 5e, indicating a charge balance was obtained via

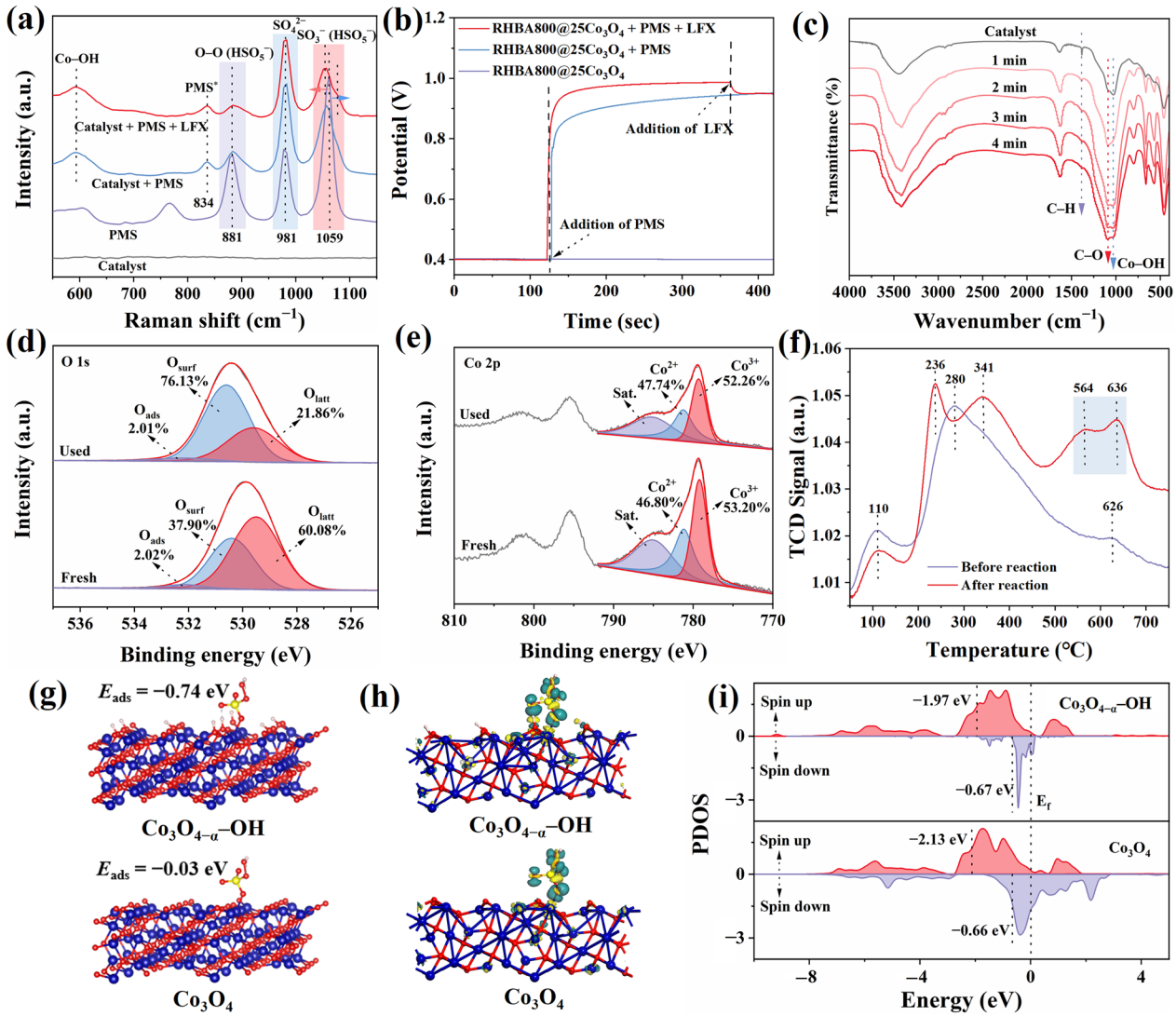

Fig. 5 **a** In situ Raman spectra of RHBA800@25Co_3O_4 after the addition of PMS and LFX; **b** Chronopotentiometry curves upon the addition of PMS and LFX; **c** In situ FT-IR spectra of catalyst in RHBA800@25Co_3O_4 + PMS system; XPS spectra of **d** O 1s and **e** Co 2p for fresh and used RHBA800@25Co_3O_4; **f** CO_2-TPD profiles of RHBA800@25Co_3O_4 before and after degradation; **g** Adsorption energy of PMS on RHBA800@25Co_3O_4 surface during PMS activation; **h** Charge differential density distribution of PMS on RHBA800@25Co_3O_4 during degradation (Dark green represents electron-acquiring capability and yellow represents electron-supplying capability); **i** Partial density of states (PDOS) plots of Co 3d orbital on RHBA800@25Co_3O_4 surface during PMS activation (Experimental conditions: $[Catalysts]_0 = 0.05$ g L^{-1}, $[PMS]_0 = 0.15$ mM, $[LFX]_0 = 10$ mg L^{-1})

Co^{2+}–Co^{3+}–Co^{2+} redox during the PMS activation on the RHBA800@25Co_3O_4 surface.

To further explore the catalytic mechanism of RHBA800@25Co_3O_4, the catalysts after degradation were characterized with CO_2-temperature-programmed desorption (CO_2-TPD). As presented in Fig. 5f, the profile of the used catalyst exhibited a significant CO_2 desorption peak in the high-temperature region (500–700 ℃), indicating that the catalyst after degradation possessed not only moderately basic sites compared with the fresh catalyst but also strongly basic sites (Li et al. 2025). These apparent changes confirmed the presence of electron transfer on the catalyst surface, and the O_{latt} induced the reaction to generate $CoOH^+$ in $Co_3O_{4-\alpha}$–OH during the degradation process. It is well-known that $CoOH^+$ is the key active intermediate in PMS activation (Qi et al. 2022), and the adsorption energy (E_{ads}) of PMS was demonstrated to be lower on $Co_3O_{4-\alpha}$–OH via density functional theory (DFT) calculation (Fig. 5g). Compared to the original Co_3O_4, the Co species in $Co_3O_{4-\alpha}$–OH showed a larger charge density difference, further suggesting the importance of $CoOH^+$

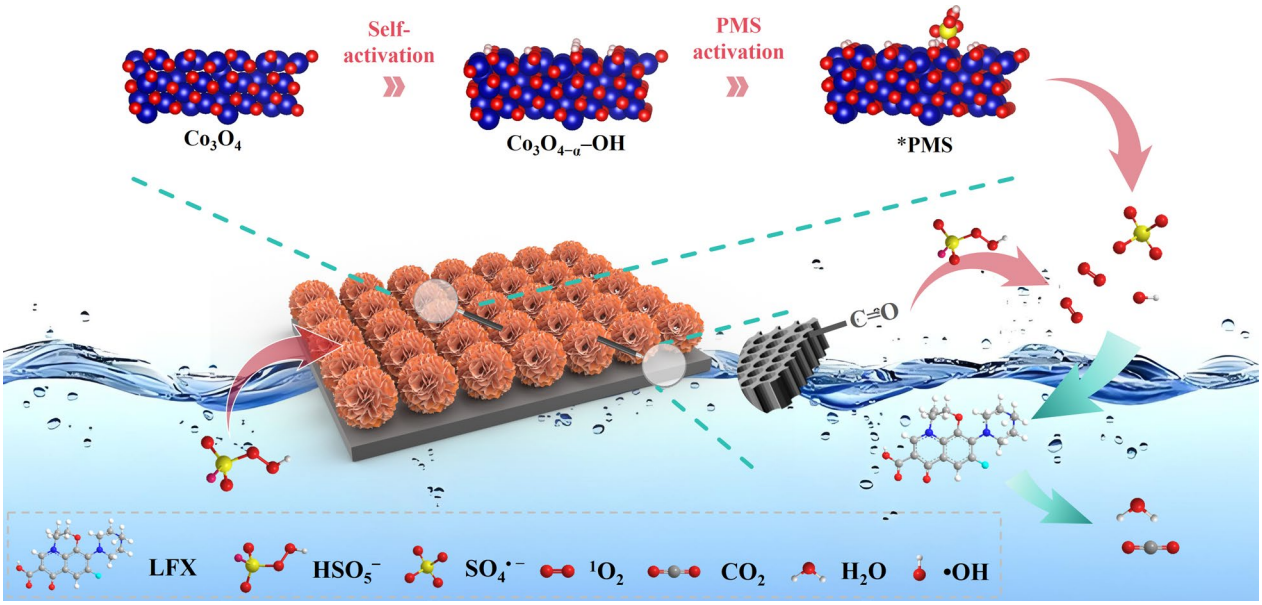

Fig. 6 Possible degradation mechanism proposed in RHBA800@25Co_3O_4 + PMS system

formation in adjusting the electronic structure during PMS activation (Fig. 5h). Meanwhile, the partial density of states (PDOS) of d-band center for Co was closer to Fermi level (E_f), suggesting the stronger adsorption of PMS and favoring its activation onto $Co_3O_{4-\alpha}$–OH (Fig. 5i). Therefore, the transformation of $CoOH^+$ from O_{latt} on the Co_3O_4 surface is believed to be more prone to generating ROS during the reaction, which will accelerate the degradation process. According to the above analysis, the possible degradation mechanism is proposed in Fig. 6.

3.4 Evaluation of RHBA800@25Co_3O_4 + PMS in practical applications

To investigate the degradation capacity of RHBA800@25Co_3O_4 + PMS towards various antibiotics, the removal efficiency of four kinds of antibiotics was explored. As exhibited in Fig. 7a, most of the antibiotics including ciprofloxacin (CIP), tetracycline (TC), and sulfadiazine (SDZ) were completely degraded within 4 min. In addition, the degradation efficiency of LFX in a variety of real-world aquatic environments was also investigated, including tap water, lake water, and secondary effluent from a sewage treatment plant (Text S7 and Table S3). As presented in Fig. 7b, the removal efficiencies of LFX were 100%, 91.96%, 100% and 94.90% in ultrapure water, lake water, tap water, and secondary effluent from the sewage treatment plant within 2 min, respectively. This demonstrates that RHBA800@25Co_3O_4 + PMS exhibits excellent resistance to interference from both organic and inorganic substances in diverse aquatic environments, delivering satisfactory treatment performance. These results indicate that RHBA800@25Co_3O_4 + PMS system possesses great potential for the removal of various antibiotics and high suitability for practical application.

Additionally, a self-developed fixed-bed reactor was built (Text S8 and Fig. 7f), and the fixed-bed experiment was conducted to test the catalytic performance (Fig. 7c). As presented, long-term PMS activation achieved significantly higher degradation efficiency for LFX compared to quartz sand adsorption, and the degradation efficiency maintained stability even after 72 h of continuous operation. Meanwhile, the leaching amount of Co ions in the effluent was determined to be much lower than the national concentration limits for industrial wastewater discharge (Fig. 7d) (Wu et al. 2021; Meng et al. 2025), and an extremely low concentration of metal ions could be observed after 60 h (<50 μg L^{-1} for the WHO standard of drinking water) (Islam et al. 2018). In addition, as shown in Fig. 7e, the TOC of the final effluent was determined to be only 49.92% of that of the original solution with the PMS dosage of 0.075 mM, indicating that the RHBA800@25Co_3O_4 + PMS system possesses prominent TOC removal capacity.

3.5 LFX degradation pathways and toxicity assessment

Based on DFT calculations of the LFX molecular structure with numbered atoms (Fig. 8a), an obvious map of electrostatic potential was observed in Fig. 8b. Meanwhile, the highest occupied molecular orbital (HOMO) and lowest unoccupied molecular orbital

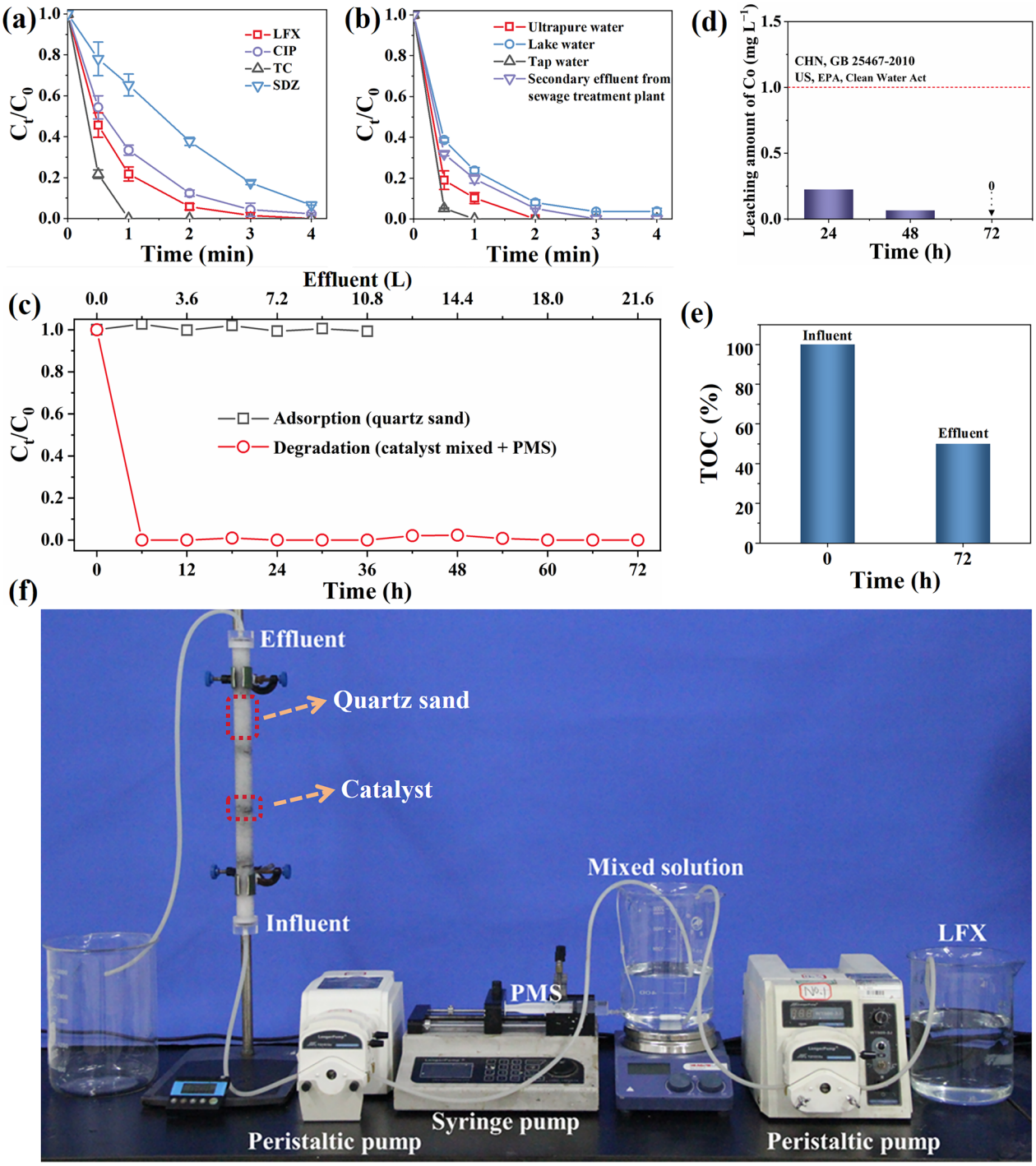

Fig. 7 **a** Degradation performance of various antibiotics and **b** the degradation performance of LFX under different real water environments in RHBA800@25Co_3O_4 + PMS system (Experimental conditions: $[Catalysts]_0 = 0.05$ g L^{-1}, $[PMS]_0 = 0.15$ mM, $[LFX]_0 = 10$ mg L^{-1} or 2 mg L^{-1}, $T = 25$ °C); **c** The removal efficiency with or without RHBA800@25Co_3O_4 in the continuous-flow test, **d** the leaching amount of metal ions and **e** TOC removal in the final effluent; **f** Photograph of the self-developed fixed-bed reactor (Experimental conditions: $[LFX]_0 = 2$ mg L^{-1}, $[PMS]_0 = 0.075$ mM, $pH_0 = 6.5$, $T = 25$ °C)

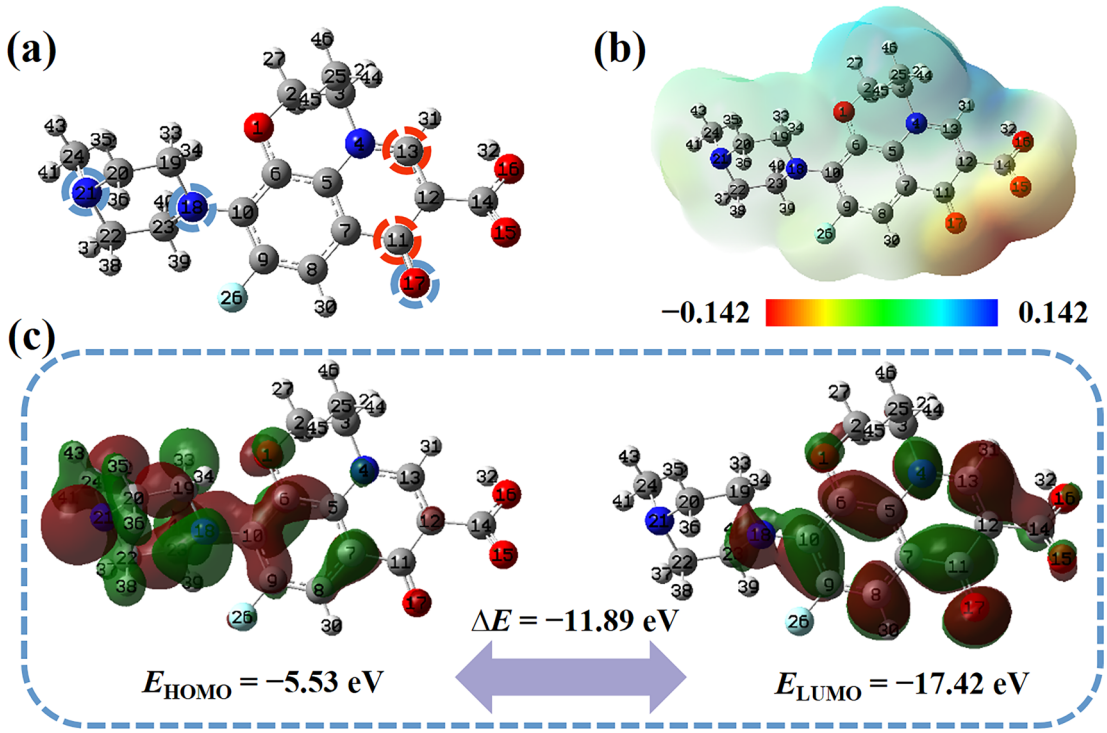

(d)

Atom	f^-	f^+	f^0	Atom	f^-	f^+	f^0
1(O)	0.0161	0.0236	0.0199	14(C)	0.0121	0.0181	0.0151
2(C)	0.0076	0.0122	0.0099	15(O)	0.0405	0.0505	0.0455
3(C)	0.0043	0.0075	0.0059	16(O)	0.0211	0.0322	0.0266
4(N)	0.0055	0.0358	0.0206	17(O)	0.058	0.0952	0.0766
5(C)	0.0132	0.0091	0.0111	18(N)	0.0912	0.0123	0.0518
6(C)	0.0296	0.0452	0.0374	19(C)	0.0231	0.003	0.0131
7(C)	0.0321	0.0061	0.0191	20(C)	0.0205	0.0056	0.013
8(C)	0.0253	0.0487	0.037	21(N)	0.0837	0.0075	0.0456
9(C)	0.0142	0.0373	0.0257	22(C)	0.0181	0.0053	0.0117
10(C)	0.0124	0.043	0.0277	23(C)	0.0226	0.0055	0.0141
11(C)	0.0147	0.0632	0.0389	24(C)	0.0212	0.0042	0.0127
12(C)	0.0164	0.0402	0.0283	25(C)	0.0042	0.0089	0.0066
13(C)	0.017	0.1042	0.0606	26(F)	0.0176	0.033	0.0253

Fig. 8 **a** Molecular structure and **b** map of electrostatic potential for LFX; **c** HOMO and LUMO model of LFX (Green clouds represent the electron deficient region and brown clouds represent electron rich regions); **d** NPA charge distribution and Fukui index of LFX

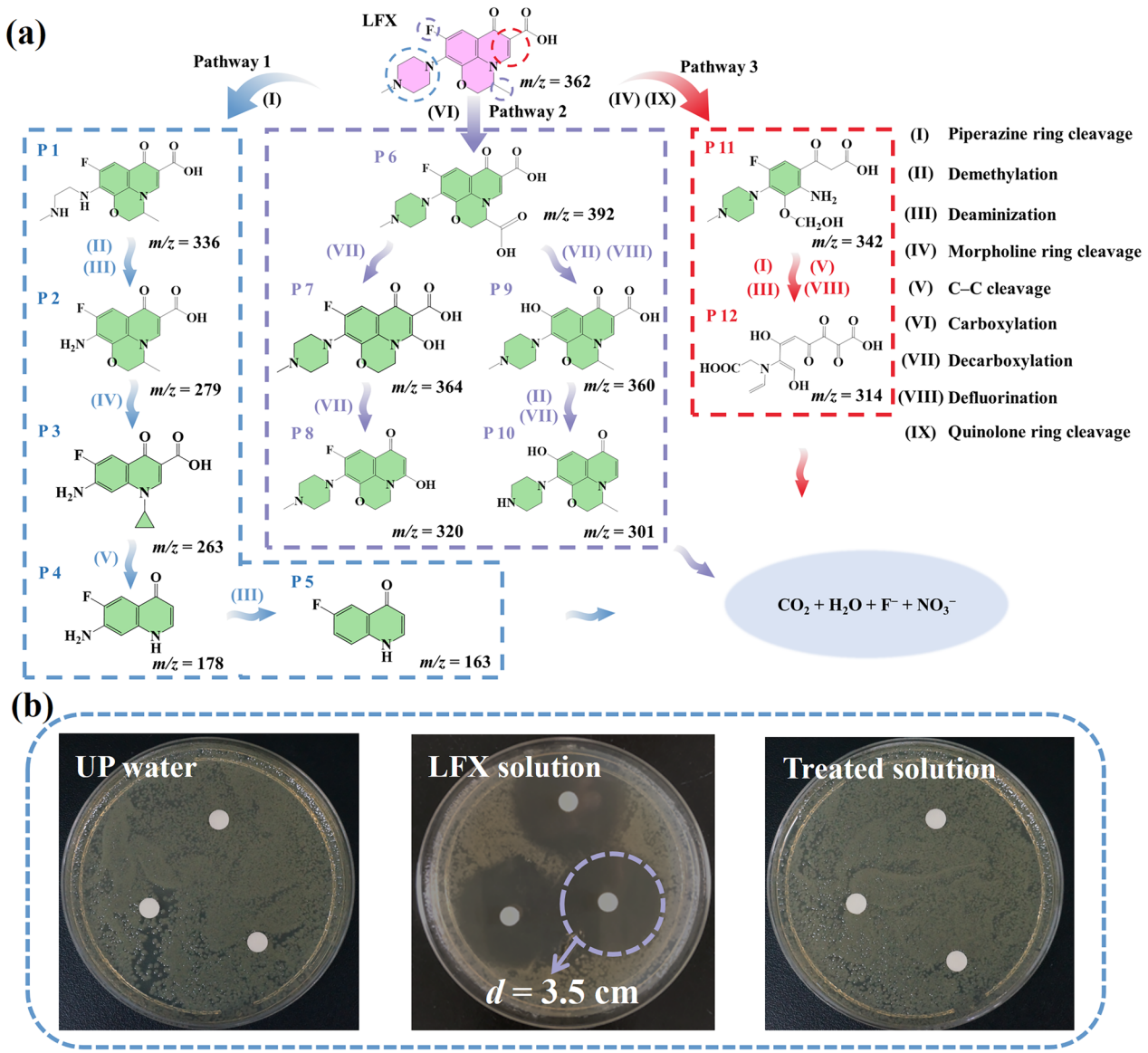

Fig. 9 **a** Proposed degradation pathways of LFX in RHBA800@25Co_3O_4 + PMS system; **b** Comparison of antibacterial experiments on *E. coli*

(LUMO) were obtained (Fig. 8c), and the Fukui index values (f^+, f^-, and f^0) of each atom in LFX were also calculated. As outlined in Fig. 8d, C13 (0.1042) and O17(0.0952) exhibited high f^+, corresponding to the reactivity of nucleophilic attack; N18(0.0912) and N21(0.0837) showed high f^-, denoting the electrophilic attack that loses electrons. Meanwhile, the C13(0.0606), O17(0.0766), N18(0.0518), and N21(0.0456) held high f^0, leading to be the position most vulnerable to ROS attack.

The intermediate products of LFX degradation in the RHBA800@25Co_3O_4 + PMS system were accurately identified with UPLC-MS/MS (Text S2 and Table S4). Combining the obtained intermediate mass spectrometry data with DFT calculation, the possible degradation pathways and intermediate products of structural information were proposed, including three main pathways: piperazine ring cleavage, defluorination, and quinolone group transformation (Fig. 9a). Pathway 1 started with piperazine ring cleavage to generate intermediate P 1 (m/z = 336) attacked by ROS, followed by a dominant oxidative degradation process. Afterward, P 2 (m/z = 279) and P 3 (m/z = 263) were produced via the processes of demethylation, deaminization, and morpholine ring cleavage. Subsequently, P 4 (m/z = 178) and P 5 (m/z = 164) were generated via C–C cleavage and a

deaminization process. Pathway 2 was initiated by the carboxylation process to generate intermediate P 6 ($m/z = 392$), followed by a decarboxylation process producing P 7 ($m/z = 364$) and P 8 ($m/z = 320$). Meanwhile, P 9 ($m/z = 360$) could also be obtained via decarboxylation and defluorination processes from P 6; then P 10 ($m/z = 301$) was generated by the demethylation and decarboxylation. Pathway 3 began with quinolone ring cleavage and morpholine ring cleavage to produce the intermediate P 11 ($m/z = 342$). Thereafter, a series of decomposition processes such as piperazine ring cleavage, deaminization, C–C cleavage, and defluorination occurred, and the least toxic intermediate P 12 ($m/z = 314$) was generated finally. The aforementioned intermediates would further degrade into low-molecular-weight organic compounds, or even completely mineralize into CO_2 and H_2O. Besides, the ecotoxicity of the intermediates was analyzed with the quantitative structure–activity relationship (QSAR) method using the Toxicity Estimation Software Tool (T.E.S.T., Ver. 5.1.1.0) (Text S16 and Fig. S22) and antibacterial experiments on *Escherichia coli* (*E. coli*) culture (Text S9) (Zhang et al. 2025b). It could be found that the tablets soaked with the original LFX solution exhibited an inhibition zone of $d = 3.5$ cm (Fig. 9b), while the tablets soaked with degraded LFX solution did not show antibacterial effect on *E. coli*, demonstrating that the comprehensive toxicity decreased substantially.

4 Conclusions

To summarize, RHBAx@yCo_3O_4 was obtained via the even distribution of Co_3O_4 on the optimized RHBA, and RHBA800@25Co_3O_4 + PMS system achieved almost 100% removal efficiency of LFX in 4 min with 0.15 mM PMS in a neutral environment. Meanwhile, a distinguished catalytic capacity for CIP, TC, and SDZ was observed, and RHBA800@25Co_3O_4 showed a satisfactory performance with high anti-interference ability in various real water environments. Moreover, RHBA800@25Co_3O_4 processes a high practicability with the self-developed fixed-bed reactor, and the leaching amount of Co was close to 0 after a long-term continuous operation. The quenching experiments and in situ EPR tests proved that the degradation process mainly involved $SO_4^{\cdot-}$, ·OH, and $^1O_2$ simultaneously. Based on the XPS characterization, the O–C=O groups were demonstrated to be beneficial for the degradation process. Most importantly, lattice oxygen in Co_3O_4 was evidenced to induce the generation of $Co_3O_{4-\alpha}$–OH according to the characterizations of in situ Raman, in situ FT-IR, and CO_2-TPD. Additionally, the E_{ads} of PMS was demonstrated to be lower on $Co_3O_{4-\alpha}$–OH (−0.74 eV), and the Co active sites in $Co_3O_{4-\alpha}$–OH exhibited a larger charge density difference, which can accelerate the electron transfer and degradation efficiency. Besides, the degradation pathways of LFX were primary piperazine ring cleavage, defluorination, and quinolone group transformation, respectively, and the aquatic toxicity of intermediates was demonstrated to be weakened. This study sheds new light on the PMS activation mechanism by biochar-loaded Co_3O_4 catalysts, and provides a theoretical basis for efficient PMS activation towards antibiotics degradation.

Supplementary Information

The online version contains supplementary material available at https://doi.org/10.1007/s42773-026-00634-8.

Additional file 1.

Acknowledgements
We gratefully appreciate the financial support from the National Key Research & Development Program of China (2021YFA1202700), China Postdoctoral Science Foundation (2024M763193), International Partnership Program of the Chinese Academy of Sciences (322GJHZ2022035MI), the Fujian Province Natural Science Foundation of China (2025J01257 and 2026J008297), and the Youth Innovation Promotion Association CAS (2022308 and 2023320).

Author contributions
Jian Zhang: Investigation, Methodology, Writing – original draft preparation. Jiafang Xie: Supervision, Investigation, Writing – reviewing and editing, Funding acquisition. Shuhui Zhu: Investigation, Methodology. Jiacheng E. Yang: Formal analysis and investigation, Funding acquisition. Bo Weng: Formal analysis and investigation. Yuming Zheng: Resources, Supervision, Funding acquisition. All authors read and approved the final manuscript.

Funding
This study was financially supported by the National Key Research & Development Program of China (2021YFA1202700), China Postdoctoral Science Foundation (2024M763193), International Partnership Program of the Chinese Academy of Sciences (322GJHZ2022035MI), the Fujian Province Natural Science Foundation of China (2025J01257 and 2026J008297), and the Youth Innovation Promotion Association CAS (2022308 and 2023320).

Data availability
The data supporting the findings of the study are included in the main text and Supporting Information files. Raw data can be obtained from the corresponding author upon request.

Declarations

Competing interests
The authors declare that they have no known competing financial interests or personal relationships that could have appeared to influence the work reported in this paper.

Author details
[1]State Key Laboratory of Advanced Environmental Technology, Institute of Urban Environment, Chinese Academy of Sciences, Xiamen 361021, Fujian, China. [2]University of Chinese Academy of Sciences, Beijing 100049, China.

Received: 11 September 2025 Revised: 12 February 2026 Accepted: 14 May 2026
Published online: 16 June 2026

References

Bao X, Zhou L, Liu B, Zhang G, Fang Y, Zeng Y (2025) Peroxydisulfate activation by one-step pyrolysis iron-rich sludge biochar for tetracycline removal in water: performance, mechanism and degradation pathway. Biochar 7:87. https://doi.org/10.1007/s42773-025-00471-1

Bhagia S, Ďurkovič J, Lagaňa R, Kardošová M, Kačík F, Cernescu A, Schäfer P, Yoo CG, Ragauskas AJ (2022) Nanoscale FTIR and mechanical mapping of plant cell walls for understanding biomass deconstruction. ACS Sustain Chem Eng 10:3016–3026. https://doi.org/10.1021/acssuschemeng.1c08163

Chen C, Liu L, Guo J, Zhou L, Lan Y (2019) Sulfur-doped copper-cobalt bimetallic oxides with abundant Cu(I): a novel peroxymonosulfate activator for chloramphenicol degradation. Chem Eng J 361:1304–1316. https://doi.org/10.1016/j.cej.2018.12.156

Chen L, Duan J, Du P, Sun W, Lai B, Liu W (2022) Accurate identification of radicals by in-situ electron paramagnetic resonance in ultraviolet-based homogenous advanced oxidation processes. Water Res 221:118747. https://doi.org/10.1016/j.watres.2022.118747

Chen H, Yu Z, Sun W, Li T, Zhang J, Qiu Z, Younas M (2024a) Degradation of tetracycline through peroxymonosulfate activation with Co/Fe-LDH modified magnetic hydrochar: synergistic effect and low toxicity. Sep Purif Technol 351:128023. https://doi.org/10.1016/j.seppur.2024.128023

Chen X, Zhou Y, He J, Pillai SC, Li N, Xu S, Li J, Chen X, Wang H (2024b) Elevated efficiency in tartrazine removal from wastewater through boron-doped biochar: enhanced adsorption and persulfate activation. Biochar 6:79. https://doi.org/10.1007/s42773-024-00377-4

Gao S, Li T, Zhao X, Hu G, Cui X, Pan L, Wågberg T (2025) Heterogeneous cobalt-based catalysts for boosting peroxymonosulfate activation: a review on cobalt-ion leaching inhibition strategies. Clean Chem Eng 11:100173. https://doi.org/10.1016/j.clce.2025.100173

Georgin J, Franco D, Meili L, Bonilla-Petriciolet A, Kurniawan T, Imanova G, Demir E, Ali I (2024) Environmental remediation of the norfloxacin in water by adsorption: advances, current status and prospects. Adv Colloid Interface Sci 324:103096. https://doi.org/10.1016/j.cis.2024.103096

Gong C, Zhao L, Li D, He X, Chen H, Du X, Wang D, Fang W, Zeng X, Li W (2023) In-situ interfacial engineering of $Co(OH)_2$/Fe_7Se_8 nanosheets to boost electrocatalytic water splitting. Chem Eng J 466:143124. https://doi.org/10.1016/j.cej.2023.143124

Hu C, Feng J, Zhou N, Zhu J, Zhang S (2021) Hydrochar from corn stalk used as bio-asphalt modifier: high-temperature performance improvement. Environ Res 193:110157. https://doi.org/10.1016/j.envres.2020.110157

Huang Q, Zhang W, Li F, Zhang M, Li Q, Yang J (2024) Highly efficient peroxymonosulfate activation by molten salt-assisted synthesis of magnetic Mn–Fe_3O_4 supported mesoporous biochar composites for SDZ degradation. ACS EST Water 4:4591–4603. https://doi.org/10.1021/acsestwater.4c00599

Islam MdA, Morton DW, Johnson BB, Pramanik BK, Mainali B, Angove MJ (2018) Opportunities and constraints of using the innovative adsorbents for the removal of cobalt(II) from wastewater: a review. Environ Nanotechnol Monit Manag 10:435–456. https://doi.org/10.1016/j.enmm.2018.10.003

Ji X, Huang J-W, Liu W-J, Yu H-Q (2021) Pyrolysis of biomass wastes to N-doped biochar-stabilized Co nanoparticles for efficient pollutant degradation via peroxymonosulfate activation. ACS EST Eng 1:1715–1724. https://doi.org/10.1021/acsestengg.1c00327

Jiang J, Shi W, Song S, Hao Q, Fan W, Xia X, Zhang X, Wang Q, Liu C, Yan D (2014) Solvothermal synthesis and electrochemical performance in super-capacitors of Co_3O_4/C flower-like nanostructures. J Power Sources 248:1281–1289. https://doi.org/10.1016/j.jpowsour.2013.10.046

Li R, Lu X, Yan B, Li N, Chen G, Cheng Z, Hou L, Wang S, Duan X (2022) Sludge-derived biochar toward sustainable peroxymonosulfate activation: regulation of active sites and synergistic production of reaction oxygen species. Chem Eng J 440:135897. https://doi.org/10.1016/j.cej.2022.135897

Li B, Liu Y, Hu K, Dai Q, Chen C, Duan X, Wang S, Wang Y (2024a) Spin-regulated Fenton-like catalysis for nonradical oxidation over metal oxide@carbon composites. Adv Funct Mater 34:2401397. https://doi.org/10.1002/adfm.202401397

Li H, Qin X, Wang K, Ma T, Shang Y (2024b) Insight into metal-based catalysts for heterogeneous peroxymonosulfate activation: a critical review. Sep Purif Technol 333:125900. https://doi.org/10.1016/j.seppur.2023.125900

Li Y, Wang K, Wang Z, Wang X, Chu X, Zhang R, Song S, Zhang H, Wang X (2025) Ultra-fast synthesis of composite oxide-supported transition metal alloy as an advanced catalyst for ammonia decomposition. Adv Energy Mater 15:2405296. https://doi.org/10.1002/aenm.202405296

Lu F, Chen Y, Huang J, Lin J, Zhang Y, Xu L, Gan L, Yan M, Gong H (2025) Peroxymonosulfate activation by peanut shell biochar-doped $BiFeO_3$ composite to remove antibiotic resistant bacteria from aquaculture wastewater. Biochar 7:104. https://doi.org/10.1007/s42773-025-00497-5

Meena V, Swami D, Chandel A, Joshi N, Prasher SO (2025) Selected emerging contaminants in water: global occurrence, existing treatment technologies, regulations and associated risk. J Hazard Mater 483:136541. https://doi.org/10.1016/j.jhazmat.2024.136541

Meng H, Zhou J, Zhang Y, Cui J, Chen Y, Zhong W, Chen Y, Jia CQ (2025) Single-atom Co-N_3 sites induce peroxymonosulfate activation for acetaminophen degradation via nearly 100 % internal electron transfer process. Appl Catal B Environ 366:125038. https://doi.org/10.1016/j.apcatb.2025.125038

Mo F, Song C, Zhou Q, Xue W, Ouyang S, Wang Q, Hou Z, Wang S, Wang J (2023) The optimized Fenton-like activity of Fe single-atom sites by Fe atomic clusters–mediated electronic configuration modulation. Proc Natl Acad Sci U S A 120:e2300281120. https://doi.org/10.1073/pnas.2300281120

Oberlé K, Capdeville M, Berthe T, Budzinski H, Petit F (2012) Evidence for a complex relationship between antibiotics and antibiotic-resistant *Escherichia coli*: from medical center patients to a receiving environment. Environ Sci Technol 46:1859–1868. https://doi.org/10.1021/es203399h

Patil DJ, Grewal HS (2025) Comparative study of heterogeneous activation of H_2O_2 and peroxymonosulfate over nanoporous $ZnFe_2O_4$ for dye degradation via batch and continuous-flow channel approach. J Water Process Eng 75:108007. https://doi.org/10.1016/j.jwpe.2025.108007

Qi J, Yang X, Pan P-Y, Huang T, Yang X, Wang C-C, Liu W (2022) Interface engineering of $Co(OH)_2$ nanosheets growing on the $KNbO_3$ perovskite based on electronic structure modulation for enhanced peroxymonosulfate activation. Environ Sci Technol 56:5200–5212. https://doi.org/10.1021/acs.est.1c08806

Schlumberger C, Thommes M (2021) Characterization of hierarchically ordered porous materials by physisorption and mercury porosimetry—A tutorial review. Adv Mater Interfaces 8:2002181. https://doi.org/10.1002/admi.202002181

Song J, Zhao C, Cao X, Cheng W (2023) Enhanced catalytic degradation of antibiotics by peanut shell-derived biochar-Co_3O_4 activated peroxymonosulfate: An experimental and mechanistic study. Process Saf Environ Prot 171:423–436. https://doi.org/10.1016/j.psep.2023.01.036

Tian W, Lin J, Tian Z, Ncube S, Zhang H, Cortés E, Sun H, Wang S (2025) Biomass native structure into functional carbon-based catalysts for Fenton-like reactions. Adv Funct Mater. https://doi.org/10.1002/adfm.202508759

Wang L, Lan X, Peng W, Wang Z (2021) Uncertainty and misinterpretation over identification, quantification and transformation of reactive species generated in catalytic oxidation processes: a review. J Hazard Mater 408:124436. https://doi.org/10.1016/j.jhazmat.2020.124436

Wang Y, Peng W, Wang J, Chen G, Li N, Song Y, Cheng Z, Yan B, Hou L, Wang S (2022) Sulfamethoxazole degradation by regulating active sites on distilled spirits lees-derived biochar in a continuous flow fixed bed peroxymonosulfate reactor. Appl Catal B Environ 310:121342. https://doi.org/10.1016/j.apcatb.2022.121342

Wang B, Sui Q, Liu H, Yu G, Qu J (2024a) Promoting environmental risk assessment and control of emerging contaminants in China. Engineering 37:13–17. https://doi.org/10.1016/j.eng.2024.03.010

Wang M, Zhang Y, Dong S, Li N, Xu Q, Li H, Lu J, Chen D (2024b) Self-floating polymer microreactor for high-efficiency synergistic CO_2 photoreduction and antibiotic degradation in one photoredox cycle. Adv Funct Mater 34:2408831. https://doi.org/10.1002/adfm.202408831

Wang H, Wang D, Sun C, Zhao X, Xu C, Li Z, Hou Y, Lei L, Yang B, Duan X (2025) Oriented generation of $^1O_2$ from peroxymonosulfate via Co_3O_4 facet engineering. Appl Catal B Environ 364:124854. https://doi.org/10.1016/j.apcatb.2024.124854

Weng B, Zhang M, Lin Y, Yang J, Lv J, Han N, Xie J, Jia H, Su B-L, Roeffaers M, Hofkens J, Zhu Y, Wang S, Choi W, Zheng Y-M (2025) Photo-assisted technologies for environmental remediation. Nat Rev Clean Technol 1:201–215. https://doi.org/10.1038/s44359-025-00037-1

Wu J, Cao M, Tong D, Finkelstein Z, Hoek EMV (2021) A critical review of point-of-use drinking water treatment in the United States. Npj Clean Water 4:40. https://doi.org/10.1038/s41545-021-00128-z

Yu T, Wang Z, Li H, Zheng K, Luo J, Liu H, Li Y, Ai L, Wang J, Song Y, Ye Z, Zhang Y, Wang H, Chen X, Chen Y (2024) MFe_2O_4/biochar composites in persulfate-advanced oxidation process for antibiotic treatment: a mini review. J Water Process Eng 68:106535. https://doi.org/10.1016/j.jwpe.2024.106535

Zhang X, Wei J, Wang C, Wang L, Guo Z, Song Y (2024) Recent advance of Fe-based bimetallic persulfate activation catalysts for antibiotics removal: performance, mechanism, contribution of the key ROSs and degradation pathways. Chem Eng J 487:150514. https://doi.org/10.1016/j.cej.2024.150514

Zhang J, Xie J-F, Chen J-J, Li W-W, Yang JE, Zheng Y-M, Yu H-Q (2025a) Mimicking the protein: hierarchically hydrophilic $Co(OH)_2$ boosted peroxymonosulfate activation for ultrafast antibiotics degradation. Adv Funct Mater. https://doi.org/10.1002/adfm.202510022

Zhang Z-Q, Duan P-J, Bai C-W, Chen X-J, Wang J, Chen F (2025b) Surface-hydroxylated single-atom catalyst with an isolated Co-O-Zn configuration achieves high selectivity in regulating active species. Nat Commun 16:2376. https://doi.org/10.1038/s41467-025-57560-9

Zhao X, Zhang Z (2025) Heterogeneous peroxymonosulfate-based advanced oxidation mechanisms: new wine in old bottles? Environ Sci Technol 59:5913–5924. https://doi.org/10.1021/acs.est.4c11311

Zhao J, Li F, Wei H, Ai H, Gu L, Chen J, Zhang L, Chi M, Zhai J (2021) Superior performance of $ZnCoO_x$/peroxymonosulfate system for organic pollutants removal by enhancing singlet oxygen generation: the effect of oxygen vacancies. Chem Eng J 409:128150. https://doi.org/10.1016/j.cej.2020.128150

Zhou Q, Song C, Wang P, Zhao Z, Li Y, Zhan S (2023) Generating dual-active species by triple-atom sites through peroxymonosulfate activation for treating micropollutants in complex water. Proc Natl Acad Sci USA 120:e2300085120. https://doi.org/10.1073/pnas.2300085120

Zou J, Fan C, Jiang Y, Liu X, Zhou W, Xu H, Huang L (2021) A preliminary study on assessing the Brunauer-Emmett-Teller analysis for disordered carbonaceous materials. Micro Meso Mater 327:111411. https://doi.org/10.1016/j.micromeso.2021.111411